Geochemical Perspectives Letters

Xenon compatibility in magmatic processes: Hadean to current contexts

Q. Chen[1], C. Sanloup[1*], D. Horlait[2], G. Shen[3]

https://doi.org/10.7185/geochemlet.2413

Abstract

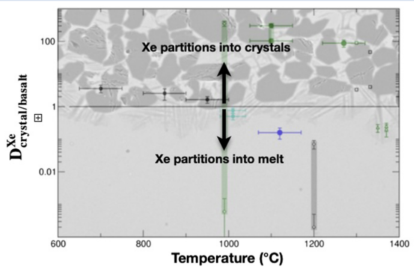

Xenon (Xe) behaviour in petrological processes, albeit essential to constrain mantle ingassing and degassing models, is elusive due to its volatile nature, and lack of direct investigation at the pressures (P) and temperatures (T) relevant to magma formation and crystallisation at depth. Xenon stands out amongst noble gases due to its unique reactivity with silicates of the lower crust and upper mantle, which could at least partially explain that published mineral/melt partitioning coefficients span up to six orders of magnitude. We report partition coefficients of Xe using *in situ* X-ray fluorescence at high P and T, and mass spectrometry analyses. Xenon is found to be moderately incompatible in anorthite-clinopyroxene mix in equilibrium with basalt (partition coefficient value of 0.16 ± 0.06), and compatible in olivine in equilibrium with basalt (partition coefficients in the range 88 ± 22 to 302 ± 46). While Xe is, thus, concentrated in basaltic melts coexisting with crystallising pyroxenes and feldspars, it is strongly retained in olivine at depth. Consequently, Xe originally contained in solid Earth has been preferentially retained at depth throughout Earth's history, from the magma ocean stages to present day partial mantle melting processes.

Received 12 October 2023 | Accepted 15 March 2024 | Published 22 April 2024

Introduction

Noble gases provide unique clues to unravel the geochemical evolution of volatile elements upon Earth's formation to present day geodynamics (Ozima *et al.*, 2002 and references therein), assuming their inertness and volatile behaviour. Xenon is also unique for its enigmatic atmospheric depletion relative to lighter noble gases (Anders and Owen, 1977), known as the 'Xe paradox', and its strong depletion in light isotopes (Krummenacher *et al.*, 1962). Atmospheric escape and trapping-at-depth scenarios have been proposed to explain both observations (Ardoin *et al.*, 2022; Broadley *et al.*, 2022; Rzeplinski *et al.*, 2022 and references therein), and are not exclusive. Atmospheric escape models stem from the fact that Xe is the easiest to ionise amongst noble gases and to investigate regarding how this could be triggered by extreme UV radiation of the young Sun if sufficient amount of hydrogen or organic matter were present. However, the main challenge is how to lift the heavy Xe through the atmosphere up to levels where it can be lost (Zahnle *et al.*, 2019). Trapping-at-depth scenarios, in turn, suffer from a lack of knowledge on Xe petrological behaviour. Noble gases partitioning between major minerals and melt is indeed a debated issue, with Xe spanning the largest range amongst noble gases crystal/melt partitioning data (noted as $D^{Xe}_{crystal/melt}$), with up to 6 orders of magnitude from 6×10^{-4} to 351 for $D^{Xe}_{olivine/basalt}$ (Hiyagon and Ozima, 1986; Broadhurst *et al.*, 1992; Heber *et al.*, 2007).

The published experimental $D^{Xe}_{crystal/melt}$ values were obtained from samples brought to high T, equilibrated with a noble gas medium either at atmospheric P or ~110 MPa, and quenched to room conditions for chemical analysis. A few experiments were carried out at higher P up to 1.5 GPa (Hiyagon and Ozima, 1986) but with only adsorbed air on starting sample as noble gas source. After correction for eventual melt inclusions in crystals, the very large range of $D^{Xe}_{crystal/melt}$ values partly results from the interpretation of bubbles in minerals, *i.e.* whether they should be excluded from measurements or not. Indeed, while noble gas content in melts is homogeneous, such is not the case in minerals, with almost systematic reports of heterogeneous distribution of heavy noble gases, often at the micron or sub-micron scale (Hiyagon and Ozima, 1986; Broadhurst *et al.*, 1992; Heber *et al.*, 2007). Some data were discarded on this ground, despite sometimes clear elemental fractionation from the original gas (Hiyagon and Ozima, 1986), which is not expected for passively trapped gas. Indeed, Xe was observed to retro-diffuse out of olivine in high P experiments upon T-quenching (Sanloup *et al.*, 2011), an exsolution process that could explain at least part of the bubbles observed on quenched samples. It is therefore very challenging to interpret the heterogeneous distribution of Xe in quenched minerals recovered from experiments.

Another source of controversy arises from the impact of noble gases adsorption on minerals, *i.e.* whether or not it is significant in experiments, and therefore if it should be corrected

1. Institut de Minéralogie, de Physique des Matériaux et de Cosmochimie, Sorbonne Université, CNRS, Paris, 75005, France
2. LP2I, UMR5797, Université de Bordeaux, CNRS, Gradignan, 33170, France
3. HPCAT, X-ray Science Division, Argonne National Laboratory, Argonne, 60439, IL, USA
* Corresponding author (email: chrystele.sanloup@sorbonne-universite.fr)

for or not. Step heating experiments show that heavy noble gases are tightly bound in minerals, with largest fractions being released above 1000 °C (Hiyagon and Ozima, 1986), arguing against physical adsorption.

Last but not least, datasets are difficult to compare due to the different compositions used for both melts and crystals (Table 1). For instance, olivine-melt experiment compositions range from synthetic Fe-free forsterite/61 % SiO_2-rich melt (Heber *et al.*, 2007) to natural olivine/basalt (Hiyagon and Ozima, 1986). It is, nonetheless, established that melt composition strongly affects trace element partitioning (Schmidt *et al.*, 2006), with one order of magnitude difference between gabbroic and granitic melts, an effect also expected to be strong for noble gases based on solubility values in melts (Carroll and Stolper, 1993; Schmidt and Keppler, 2002).

Facing these experimental controversies, the peridotitic database shows an enrichment in Xe over other noble gases in xenoliths (Hennecke and Manuel, 1975; Poreda and Farley, 1992; Czuppon *et al.*, 2009). Consistently, natural measurements of Xe mineral/basalt partitioning obtained by analysing parent and partially crystallised magmas (Batiza *et al.*, 1979), or coexisting magma and olivine crystals (Kaneoka *et al.*, 1983), show Xe compatibility with $D^{Xe}_{crystal/basalt}$ a few-fold above unity. Natural measurements must, nonetheless, be considered with caution (Carroll and Draper, 1994) due to potential magma degassing processes if minerals and melt did not re-equilibrate, and/or if crystals contain vapour inclusions (Kaneoka *et al.*, 1983), which as for experiments are difficult to interpret.

To circumvent these problems, we have recently developed a new method combining synchrotron X-ray fluorescence and diffraction techniques with large volume presses (Chen *et al.*, 2022). The method was first tested on crystal/felsic melt Xe partitioning, and Xe was found to be moderately incompatible to compatible, with a *T*-dependent behaviour (0.50 ± 0.20 for $D^{Xe}_{plagioclase/melt}$ at 1010 °C to 3.46 ± 0.25 for $D^{Xe}_{jadeite/melt}$ at 700 °C). This method is applied here to a Paris-Edinburgh press energy-dispersive set-up, which has the additional advantage of being optimised for the observation of diffuse X-ray scattering signal from melts.

Mineral/Melt Xenon Partitioning Measurements

We measured Xe partition coefficient between olivine and basalt, and between feldspar-clinopyroxene mix and basalt, in order to target Xe petrological behaviour in early Hadean contexts (*e.g.*, magma oceans in planetary embryos) and present day subduction zone contexts respectively. Xenon crystal/melt partition coefficients were measured by means of *in situ* synchrotron X-ray diffraction and X-ray fluorescence simultaneously collected on the same spectrum, using an energy-dispersive set-up and a Paris-Edinburgh press to generate high *P*-*T* conditions (Supplementary Information). The starting sample (Supplementary Information) is a synthetic glass relevant for lunar-like magma ocean at the stage of anorthite crystallisation, doped by high *P*-*T* synthesis with 0.05 wt. % Xe (Table S-1), *i.e.* well below Xe solubility in tholeiitic melt (Schmidt and Keppler, 2002) of 0.41 wt. % at 2 GPa to avoid supersaturation, while being high enough for the Xe fluorescence signal to be significantly above noise level. The starting sample is used either pure to mimic planetesimal magma ocean stages or mixed with 10 wt. % labradorite feldspar to get an analogue of high alumina basalts, relevant for present day subduction zone settings. At each targeted *P*, *T* was first raised until recrystallisation, further raised until full remelting, and lowered until crystals grew in equilibrium with melt to ensure chemical equilibrium. The sample was then scanned perpendicularly to the X-ray beam in order to probe either pure melt or crystallised areas. For the olivine/basalt experiments, crystals were efficiently segregated from melt due to their density difference. This was not the case of the pyroxene-feldspar/basalt experiments for which it was not possible to probe only crystals, and the fraction of melt *vs.* crystals in crystal-rich areas was determined from the X-ray diffraction signal (Supplementary Information). Xenon content in pure melt or crystals was obtained from the Xe K_α fluorescence intensity signal in the fully molten sample pattern and the relevant pattern, either pure melt or crystals, at crystal-melt equilibrium (Supplementary Information). If a pure crystal pattern could not be obtained, Xe content in crystals from mixed crystals + melt pattern was obtained using mass-balance calculation from Xe K_α fluorescence intensity in crystal-rich area and local melt fraction obtained from X-ray diffraction signal (Eq. S-3).

For basaltic melt in equilibrium with feldspar and pyroxene, Xe was enriched in the melt as seen by the stronger Xe fluorescence signal (Fig. 1) and the derived partition coefficient (0.16 ± 0.06; Table 2). Crystal growth partly occurred upon quenching to room *T* (see microlithic texture of sample in Fig. S-3), hence it is difficult to have a proper estimate of feldspar *vs.* pyroxene at high *P*-*T* conditions, and oriented crystal growth prevents estimate from *in situ* energy-dispersive X-ray diffraction data. Nonetheless, due to the low global *D* value, Xe had to be incompatible with both pyroxene and feldspar at our experimental conditions, consistent with the reported *T*-dependence of *D* for clinopyroxene/felsic melt (Chen *et al.*, 2022). In contrast, Xe fluorescence signal was not detected in basalt coexisting with olivine (Fig. 1), which implies a lower limit of 80 for $D^{Xe}_{olivine/basalt}$, taking the noise oscillations as a maximum for Xe fluorescence signal in melt. Xenon X-ray fluorescence signal in olivine crystals is strongly affected by quenching *T* at high *P*, with a 2.9 factor decrease in intensity (Fig. 1a), indicating important—although incomplete—Xe exsolution back to room *T*, consistent with previous observation from *in situ* X-ray diffraction (Sanloup *et al.*, 2011).

To further constrain Xe concentration in melt coexisting with olivine, pieces of glass recovered from synchrotron experiments and an additional sample synthesised at similar *P*-*T* conditions (Supplementary Information) were analysed by noble gas mass spectrometry. From the additional sample, three fragments of glass and two fragments of mostly crystals could be separated, as olivine crystals had sedimented at the bottom of the capsule. Mass spectrometry analyses were done on bulk sample fragments fully melted by laser heating (Supplementary Information), revealing systematic Xe enrichment in olivine-rich fragments compared to glass. Olivine content in olivine-rich fragments is estimated at 83 ± 10 % from analyses of SEM images (Fig. S-3) using ImageJ software. Our reported values of $D^{Xe}_{olivine/basalt}$, 88(22)–302(46) (Table 2), exceed 80 as expected from the lack of Xe X-ray fluorescence signal in the melt. The lower range value was obtained using Xe content in crystals as measured from energy-dispersive X-ray data, and Xe content in glass as measured by mass spectrometry (Table S-2), which is near the 104(16) value obtained on the additional sample using mass spectrometry results only. The upper range corresponds to that value times the intensity ratio between crystals at high *P*-*T* and quenched crystals at high *P* (*i.e.* 2.9 GPa), to account for Xe exsolution from olivine crystals upon quenching.

Table 1 Compilation of literature datasets. Chemical compositions have been rounded at unity, given in wt. % for glass and mol % for gas. Analytical techniques: UV laser ablation (Heber *et al.*, 2007), step heating (Hiyagon and Ozima, 1986; Broadhurst *et al.*, 1992). Data discarded by authors due to contamination of crystals with bubbles are given in italics. For Hiyagon and Ozima (1986), glass composition is bulk sample starting composition. Data where lithium borate was added to lower melting *T* are not included, as borate modifies melt polymerisation which controls noble gases solubility. Error bars on *D* are given when available; * error equals *D* values.

Run (ref.)	Thermal treatment (duration @ °C)	*P* (GPa)	Glass composition (wt. %)	Crystal	Gas composition (mol %)	D^{Xe} (error)
olivine-melt partitioning						
V (B1992)	18 d @ 1300	10^{-4}	$54SiO_2$-$15Al_2O_3$-14MgO-17CaO	natural forsterite	5Ne-93Ar-1Kr-1Xe	90
RB587 (H2007)	1 h @ 1165 + 3 h @ 1045 + 6 h @ 990	0.1	$61SiO_2$-$15Al_2O_3$-$23Na_2O$	Mg_2SiO_4	25He-23Ne-25Ar-22Kr-5Xe	3.9×10^{-3}–*351*
RB588 (H2007)	1 h @ 1165 + 3 h @ 1045 + 6 h @ 990	0.1	$61SiO_2$-$16Al_2O_3$-$24Na_2O$	Mg_2SiO_4	25He-23Ne-25Ar-22Kr-5Xe	6×10^{-4}–*148*
RB589 (H2007)	1 h @ 1165 + 3 h @ 1045 + 6 h @ 990	0.1	$58SiO_2$-$16Al_2O_3$-$23Na_2O$	Mg_2SiO_4	25He-23Ne-25Ar-22Kr-5Xe	0
BH-257 (H1986)	3 h 23 min @ 1370	10^{-4}	$48SiO_2$-$15Al_2O_3$-10FeO-15MgO-7CaO-$1Na_2O$	$(Mg,Fe)_2SiO_4$	11He-1Ne-88Ar-0.3Kr-0.1Xe + CO_2-H_2 (0.5 to 1 ratio)	0.197(0.080)
BH-258 (H1986)	7 h 36 min @ 1370	10^{-4}	$48SiO_2$-$15Al_2O_3$-10FeO-15MgO-7CaO-$1Na_2O$	$(Mg,Fe)_2SiO_4$	11He-1Ne-88Ar-0.3Kr-0.1Xe + CO_2-H_2 (0.5 to 1 ratio)	0.240(0.069)
BH-276 (H1986)	14 h 20 min @ 1350	10^{-4}	$48SiO_2$-$15Al_2O_3$-10FeO-15MgO-7CaO-$1Na_2O$	$(Mg,Fe)_2SiO_4$	115He-1Ne-88Ar-0.3Kr-0.1Xe + CO_2-H_2 (0.5 to 1 ratio)	0.222(0.059)
HPP-1 (H1986)	10 min @ 1350	1.0	$48SiO_2$-$15Al_2O_3$-10FeO-15MgO-7CaO-$1Na_2O$	$(Mg,Fe)_2SiO_4$	air adsorbed on powder	0.14(0.05)
HPP-3 (H1986)	4 h @ 1360	1.5	$48SiO_2$-$15Al_2O_3$-10FeO-15MgO-7CaO-$1Na_2O$	$(Mg,Fe)_2SiO_4$	air adsorbed on powder	0.046(0.016)
pyroxene-melt partitioning						
IV (B1992)	18 d @ 1300	10^{-4}	$56SiO_2$-$11Al_2O_3$-15MgO-19CaO	natural diopside	5Ne-93Ar-1Kr-1Xe	3.3
V (B1992)	7 d @ 1332	10^{-4}	$56SiO_2$-$11Al_2O_3$-15MgO-19CaO	natural diopside	5Ne-93Ar-1Kr-1Xe	47
VI (B1992)	9 d @ 1332	10^{-4}	$56SiO_2$-$11Al_2O_3$-15MgO-19CaO	natural diopside	5Ne-93Ar-1Kr-1Xe	4.0
RB586 (H2007)	0 h 30 min @ 1290 + 1 h @ 1272 + 6 h @ 1200	0.1	$65SiO_2$-$14Al_2O_3$-4MgO-8CaO	$(Mg_x,Ca_y)SiO_3$	25He-23Ne-25Ar-22Kr-5Xe	0.2–*70* $\times 10^{-3}$ *
HH355 (C2022)	2 h 30 min @ 950 + 3 h 45 min @ 700	1.6	$67SiO_2$-$15Al_2O_3$-1CaO-$5Na_2O$	jadeite	Xe	3.58
HH357 (C2022)	4 h 20 min @ 850	1.7	$60SiO_2$-$18Al_2O_3$-1MgO-2CaO-$8Na_2O$	omphacite	Xe	2.54
feldspar-melt partitioning						
Cell5 (C2022)	6 h 30 min @ 1010	2.0	$63SiO_2$-$24Al_2O_3$-5CaO-$8Na_2O$	plagioclase	Xe	0.76

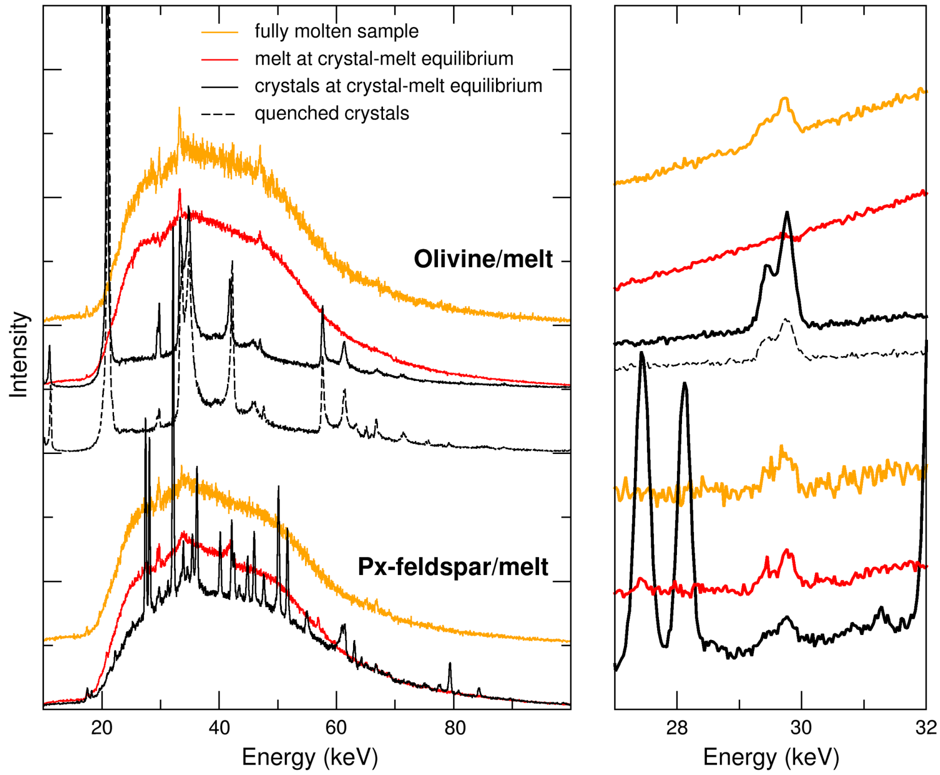

Figure 1 Energy-dispersive X-ray data sets. (Left) Full data sets collected at 10.031°. For each crystal/melt system, data collected at different *T* are vertically spaced for clarity: fully molten sample (orange), partially molten sample (red for molten zone, black for crystalline or crystal-rich zone), and quenched crystals (black dashed). Peaks at 33 keV and 47 keV are MgO diffraction peaks from the cell-assembly. (Right) Zoom on the Xe $K_{\alpha1}$ and $K_{\alpha2}$ fluorescence lines (29.4 keV and 29.7 keV). For olivine-melt experiments, data sets in the zoomed panel were collected at 4.0285° to avoid diffraction peaks from crystals overlapping with Xe fluorescence lines.

Table 2 Run conditions, coexisting phases, crystalline fraction in crystal-rich areas, Xe content in each phase (wt. %), and partitioning coefficients. Note that crystal and melt fractions do not apply to the whole sample but only to the volume probed by the X-ray beam. *Mass spectrometry measurement. Values in parentheses are errors on the last reported digits.

Run	*P* (GPa)	*T* (°C)	Phases	$X_{crystals}$	$[Xe]^{crystals}$ (wt. %)	$[Xe]^{melt}$ (wt. %)	$D^{Xe}_{crystal/melt}$
Cell2	2.0	1270	Ol + melt	100(5)	0.145(36)	$1.65(15) \times 10^{-3*}$	88(22)
PC265	1.3	1100	Ol + glass	83(10)	0.015(6)*	$1.5(8) \times 10^{-4*}$	104(16)–302(46)
Cell3	1.2	1120	An + Di + melt	34(4)	0.007(2)	0.044(9)	0.16(6)

Olivine Retains Xe in Magmatic Processes

Clinopyroxene-feldspar/melt data are broadly consistent with the *T*-trend reported for pyroxene/felsic melt under similar *P* (Chen *et al.*, 2022), and intermediate within the range of literature values at ambient or near ambient *P* (Broadhurst *et al.*, 1992; Heber *et al.*, 2007). Olivine/melt data (Fig. 2) confirm the compatible nature of Xe in olivine predicted from *ab initio* calculations (Crépisson *et al.*, 2018), are similar to ambient *P* data from Broadhurst *et al.* (1992), and correspond to the higher range from Heber *et al.* (2007). The latter study may underestimate $D^{Xe}_{olivine/basalt}$ as 1) the melt was enriched in silica (Table 1) while Xe solubility increases by a factor of five, for instance, between a MORB and a haplogranite (Leroy *et al.*, 2019), and 2) crystals with bubbles were discarded on the basis of potential contamination while, at least, some of the bubbles are expected to form upon *T*-quenching, although this effect could be restricted to high *P* conditions.

Considered together, the present high *P*-*T* clinopyroxene-feldspar/melt and olivine/melt data are consistent with the natural reports of bulk peridotite/melt partitioning coefficient a few-fold above unity from oceanic island basalts (Batiza *et al.*, 1979; Kaneoka *et al.*, 1983). The *P* effect on $D^{Xe}_{crystal/melt}$ could not be investigated here due to the limited *P*-*T* stability field of the mineralogical parageneses investigated. It further cannot be inferred from the comparison of the present and previous datasets (Fig. S-5) as data are either at ambient or near ambient *P* (10^{-4} and 0.1 GPa) or in a restricted *P*-range between 1.0 and 2.0 GPa. Additionally, the only high *P* previous dataset for olivine/melt partitioning was obtained with only air adsorbed on samples as a source of noble gases (Hiyagon and Ozima, 1986). Pressure is, nonetheless, expected to be important as Xe retention in silicates is *P*-induced. Importantly, Xe retention does not extend to lower mantle silicates (Shcheka and Keppler, 2012), consistent with the plume source being depleted in Xe compared to MORB source (Parai, 2022).

As for any element, Xe crystal chemistry controls its partitioning behaviour, and its knowledge is key to understand its

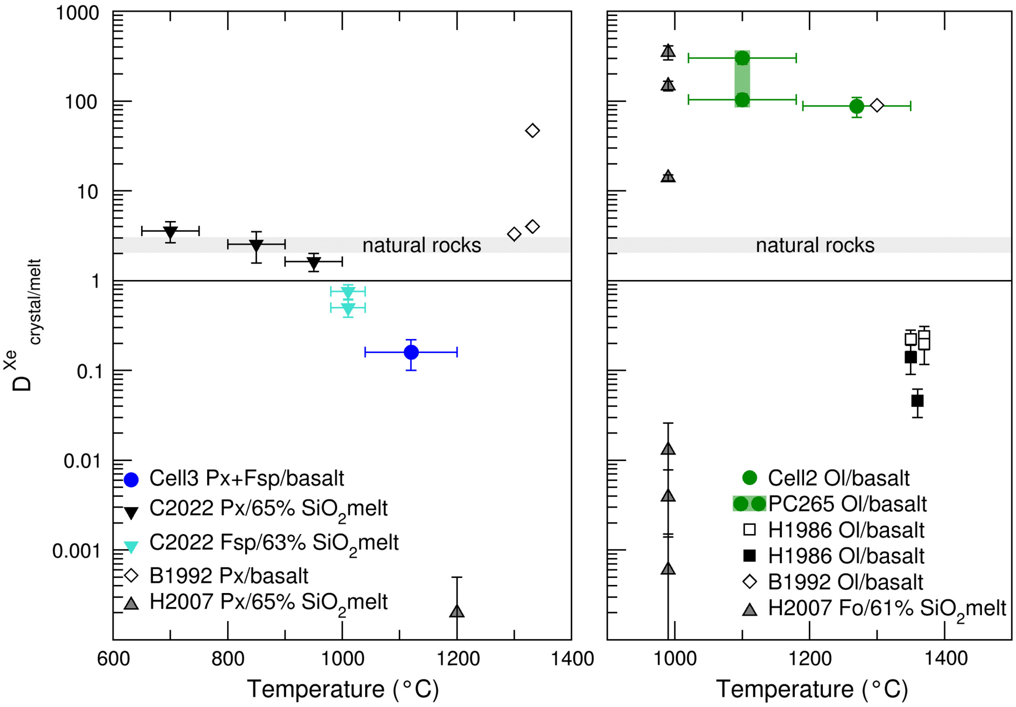

Figure 2 Summary of Xe crystal/melt partition coefficients. Data abbreviations: H1986, Hiyagon and Ozima (1986); B1992, Broadhurst *et al.* (1992); H2007, Heber *et al.* (2007); C2022, Chen *et al.* (2022); PC265, Cell2, and Cell3 are data from this study (Table 2). Empty symbols indicate room *P* data; filled symbols indicate data collected between 1.0 and 2.0 GPa (*cf.* Table 1). Note that Heber *et al.* (2007) discarded all values above unity due to the observation of gas bubbles in crystals, while at least some might form from exsolution upon quenching. Natural rocks dataset: residual rock/basalt partition coefficients from Batiza *et al.* (1979).

repartition in planetary envelopes. In magmas, noble gases enter the ring structure of silicate melts (Carroll and Stolper, 1993), eventually leading to oxidation in the case of Xe in compressed silica-rich melt (Leroy *et al.*, 2019). In minerals, the tightly bound nature of Xe leads to the suggestion that either interstitial sites or crystal vacancies are possible sites for the Xe atoms (Hiyagon and Ozima, 1986). Theoretical calculations have shown that Xe can chemically bond to oxygen in quartz (Probert, 2010; Crépisson *et al.*, 2019) and olivine (Crépisson *et al.*, 2018) under modest *P* by substituting a Si atom. This precludes the use of mineral/melt partitioning models considering Xe as a 'zero'-charge species (Brooker *et al.*, 2003). The radius of chemically bonded Xe is, indeed, much smaller than that of inert Xe, with three oxygen atoms located at 2.0 Å in a planar configuration in olivine (Crépisson *et al.*, 2018), and two nearest oxygen atoms at 2.0 Å, and two further ones at 2.3 Å in quartz (Crépisson *et al.*, 2019). Xenon crystal chemistry has not been reported for pyroxene nor feldspar but for the latter it might be similar to that in quartz, both being tectosilicates. The contrasting $D^{Xe}_{crystal/melt}$ values between olivine/basalt and pyroxene-feldspar/basalt may relate to the different local environments of Xe in these minerals.

Over the course of Earth's history, Xe should have been strongly retained in olivines crystallising from magma oceans, and in olivine-rich residues in present day mantle partial melting processes. Preferential release to the atmosphere is instead expected from high *T* (>1000 °C) crustal processes, turning to a moderate retention in pyroxenes and feldspars equilibrated with lower *T* melts such as evolved hydrous magmas in continental crust and arc contexts (Chen *et al.*, 2022). The petrological behaviour of Xe hence supports the trapping-at-depth scenario (Rzeplinski *et al.*, 2022), whereby a succession of collisions between pre-planetary embryos led to the depletion in terrestrial and Martian Xe light isotopes due to Xe trapping and oxidation in crystallising magma oceans, while over 99 % (Harper and Jacobsen, 1996) of the initial budget was expelled from growing planetesimals by exsolution from melt at low *P* in convecting magma oceans followed by atmospheric losses on a few Myr timescale. The late veneer chondritic input to the atmosphere followed by partial-only Xe degassing concomitantly with the emplacement of the continental crust led to the rising Kr/Xe ratio and progressively heavier Xe observed in Archean atmospheric samples (Broadley *et al.*, 2022) until the late veneer got overprinted, while lighter Xe in the mantle (Peron and Moreira, 2018) would result from mixing mass fractionated Xe with subducted Archean atmospheric Xe. This Archean evolution is not observed on Mars where such events did not occur. That the retention of Xe differs in minerals while its impact on isotopic fractionating is similar (Rzeplinski *et al.*, 2022) implies that Xe elemental and isotopic evolution cannot be modelled by the same Rayleigh distillation law. Indeed, Rayleigh-predicted Kr/Xe ratios for the Archean atmosphere disagree (Broadley *et al.*, 2022), a mismatch attributed to variable Xe loss over time which is challenging to reconcile with a continuous isotopic evolution.

Acknowledgements

We acknowledge K. Curtis-Benson for providing parts for cell-assemblies and arranging shipments before and after experiments, O. Boudouma for SEM measurement, N. Rivodini for EPMA analyses. Funding: Q. Chen is funded by CSC scholarship (#201806340094). HPCAT operations are supported by DOE-NNSA's Office of Experimental Sciences. The Advanced Photon Source is a U.S. Department of Energy (DOE) Office of Science User Facility operated for the DOE Office of Science by Argonne National Laboratory under Contract No. DE-AC02-06CH11357.

Editor: Anat Shahar

Additional Information

Supplementary Information accompanies this letter at https://www.geochemicalperspectivesletters.org/article2413.

Cite this letter as: Chen, Q., Sanloup, C., Horlait, D., Shen, G. (2024) Xenon compatibility in magmatic processes: Hadean to current contexts. *Geochem. Persp. Let.* 29, 57–62. https://doi.org/10.7185/geochemlet.2413

References

Anders, E., Owen, T. (1977) Mars and Earth: Origin and Abundance of Volatiles. *Science* 198, 453–465. https://doi.org/10.1126/science.198.4316.453

Ardoin, L., Broadley, M.W, Almayrac, M., Avice, G., Byrne, D.J., Tarantola, A., Lepland, A., Saito, T., Komiya, T., Shibuya, T., Marty, B. (2022) The end of the isotopic evolution of atmospheric xenon. *Geochemical Perspective Letters* 20, 43–47. https://doi.org/10.7185/geochemlet.2207

Batiza, R., Bernatowicz, T.J., Hohenberg, C.M., Podosek, F.A. (1979) Relations of noble gas abundances to petrogenesis and magmatic evolution of some oceanic basalts and related differentiated volcanic rocks. *Contributions to Mineralogy and Petrology* 69, 301–313. https://doi.org/10.1007/BF00372332

Broadhurst, C.L., Drake, M.J., Hagee, B.E., Bernatowicz, T.J. (1992) Solubility and partitioning of Ne, Ar, Kr, and Xe in minerals and synthetic basaltic melts. *Geochimica et Cosmochimica Acta* 56, 709–723. https://doi.org/10.1016/0016-7037(92)90092-W

Broadley, M.W., Byrne, D.J., Ardoin, L., Almayrac, M.G., Bekaert, D.V., Marty, B. (2022) High precision noble gas measurements of hydrothermal quartz reveal variable loss rate of Xe from the Archean atmosphere. *Earth and Planetary Science Letters* 588, 117577. https://doi.org/10.1016/j.epsl.2022.117577

Brooker, R.A., Du, Z., Blundy, J.D., Kelley, S.P., Allan, N.L., Wood, B.J., Chamorro, E.M., Wartho, J.-A., Purton, J.A. (2003) The 'zero charge' partitioning behaviour of noble gases during mantle melting. *Nature* 423, 738–741. https://doi.org/10.1038/nature01708

Carroll, M.R., Stolper, E.M. (1993) Noble gas solubilities in silicate melts and glasses: New experimental results for argon and the relationship between solubility and ionic porosity. *Geochimica et Cosmochimica Acta* 57, 5039–5051. https://doi.org/10.1016/0016-7037(93)90606-W

Carroll, M.R., Draper, D.S. (1994) Noble gases as trace elements in magmatic processes. *Chemical Geology* 117, 37–56. https://doi.org/10.1016/0009-2541(94)90120-1

Chen, Q., Sanloup, C., Bureau, H., Rzeplinski, I., Glazyrin, K., Farla, R. (2022) Probing the partitioning behaviour of Xe using *in situ* X-ray synchrotron techniques at high *P–T* conditions. *High Pressure Research* 42, 318–335. https://doi.org/10.1080/08957959.2022.2144290

Crépisson, C., Blanchard, M., Lazzeri, M., Balan, E., Sanloup, C. (2018) New constraints on Xe incorporation mechanisms in olivine from first-principles calculations. *Geochimica et Cosmochimica Acta* 222, 146–155. https://doi.org/10.1016/j.gca.2017.10.028

Crépisson, C., Sanloup, C., Blanchard, M., Hudspeth, J., Glazyrin, K., Capitani, F. (2019) The Xe-SiO_2 System at Moderate Pressure and High Temperature. *Geochemistry, Geophysics, Geosystems* 20, 992–1003. https://doi.org/10.1029/2018GC007779

Czuppon, G., Matsumoto, T., Handler, M.R., Matsuda, J.-I. (2009) Noble gases in spinel peridotite xenoliths from Mt Quincan, North Queensland, Australia: Undisturbed MORB-type noble gases in the subcontinental lithospheric mantle. *Chemical Geology* 266, 19–28. https://doi.org/10.1016/j.chemgeo.2009.03.029

Harper Jr., C.L., Jacobsen, S.B. (1996) Noble Gases and Earth's Accretion. *Science* 273, 1814–1818. https://doi.org/10.1126/science.273.5283.1814

Heber, V.S., Brooker, R.A., Kelley, S.P., Wood, B.J. (2007) Crystal-melt partitioning of noble gases (helium, neon, argon, krypton, and xenon) for olivine and clinopyroxene. *Geochimica et Cosmochimica Acta* 71, 1041–1061. https://doi.org/10.1016/j.gca.2006.11.010

Hennecke, E.W., Manuel, O.K. (1975) Noble gases in an Hawaiian xenolith. *Nature* 257, 778–780. https://doi.org/10.1038/257778b0

Hiyagon, H., Ozima, M. (1986) Partition of noble gases between olivine and basalt melt. *Geochimica et Cosmochimica Acta* 50, 2045–2057. https://doi.org/10.1016/0016-7037(86)90258-9

Kaneoka, I., Takaoka, N., Clague, D.A. (1983) Noble gas systematics for coexisting glass and olivine crystals in basalts and dunite xenoliths from Loihi Seamount. *Earth and Planetary Science Letters* 66, 427–437. https://doi.org/10.1016/0012-821X(83)90156-5

Krummenacher, D., Merrihue, C.M., Pepin, R.O., Reynolds, J.H. (1962) Meteoritic krypton and barium versus the general isotopic anomalies in xenon. *Geochimica et Cosmochimica Acta* 26, 231–249. https://doi.org/10.1016/0016-7037(62)90014-5

Leroy, C., Bureau, H., Sanloup, C., Raepsaet, C., Glazyrin, K., Munsch, P., Harmand, M., Prouteau, G., Khodja, H. (2019) Xenon and iodine behaviour in magmas. *Earth and Planetary Science Letters* 522, 144–154. https://doi.org/10.1016/j.epsl.2019.06.031

Ozima, M., Miura, Y., Podosek, F. (2002) Revisiting I-Xe systematics, an early solar system chronometer. *Geochimica et Cosmochimica Acta* 66, A576.

Parai, R. (2022) A dry ancient plume mantle from noble gas isotopes. *Proceedings of the National Academy of Sciences* 119, e2201815119. https://doi.org/10.1073/pnas.2201815119

Péron, S., Moreira, M. (2018) Onset of volatile recycling into the mantle determined by xenon anomalies. *Geochemical Perspectives Letters* 9, 21–25. https://doi.org/10.7185/geochemlet.1833

Poreda, R.J., Farley, K.A. (1992) Rare gases in Samoan xenoliths. *Earth and Planetary Science Letters* 113, 129–144. https://doi.org/10.1016/0012-821X(92)90215-H

Probert, M.I.J. (2010) An *ab initio* study of xenon retention in α-quartz. *Journal of Physics: Condensed Matter* 22, 025501. https://doi.org/10.1088/0953-8984/22/2/025501

Rzeplinski, I., Sanloup, C., Gilabert, E., Horlait, D. (2022) Hadean isotopic fractionation of xenon retained in deep silicates. *Nature* 606, 713–717. https://doi.org/10.1038/s41586-022-04710-4

Sanloup, C., Schmidt, B.C., Gudfinnsson, G., Dewaele, A., Mezouar, M. (2011) Xenon and Argon: A contrasting behavior in olivine at depth. *Geochimica et Cosmochimica Acta* 75, 6271–6284. https://doi.org/10.1016/j.gca.2011.08.023

Schmidt, B.C., Keppler, H. (2002) Experimental evidence for high noble gas solubilities in silicate melts under mantle pressures. *Earth and Planetary Science Letters* 195, 277–290. https://doi.org/10.1016/S0012-821X(01)00584-2

Schmidt, M.W., Connolly, J.A.D., Günther, D., Bogaerts, M. (2006) Element Partitioning: The Role of Melt Structure and Composition. *Science* 312, 1646–1650. https://doi.org/10.1126/science.1126690

Shcheka, S.S., Keppler, H. (2012) The origin of the terrestrial noble-gas signature. *Nature* 490, 531–534. https://doi.org/10.1038/nature11506

Zahnle, K.J., Gacesa, M., Catling, D.C. (2019) Strange messenger: A new history of hydrogen on Earth, as told by Xenon. *Geochimica et Cosmochimica Acta* 244, 56–85. https://doi.org/10.1016/j.gca.2018.09.017

Geochemical Perspectives Letters

Xenon compatibility in magmatic processes: Hadean to current contexts

Q. Chen, C. Sanloup, D. Horlait, G. Shen

Supplementary Information

The Supplementary Information includes:

- Methods
- Tables S-1 and S-2
- Figures S-1 to S-5
- MS Datasheets S-1 to S-7
- Supplementary Information References

Methods

Sample preparation

For olivine/melt partitioning experiments, starting glass (Table S-1) was prepared from reagent grade oxides and carbonates powders to reproduce the composition of lunar magma ocean at the stage of anorthite crystallisation (Sakai *et al.*, 2014). Powders were first ground and decarbonated by slowly heating in a platinum crucible in an atmospheric furnace from room temperature to 1000 °C, run for 10 hours, molten at 1500 °C for 1 hour, and then quenched in water. Recovered glass was crushed into powder again and remolten twice to ensure homogeneity. Xenon doping was done using a gas loading device (Boettcher *et al.*, 1989) to introduce Xe in a platinum capsule previously filled to one third with crushed glass, and brought to 1610 °C and 2.2 GPa for 40 minutes with a piston cylinder press (run PC202, 'Xe-doped glass' in Table S-1). For mass spectrometry analyses, an additional sample was synthesised (run PC265) using as starting composition a previously Xe-doped basaltic glass synthesised similarly to run PC202, recovered, loaded in a new Pt capsule, and brought to 1.3 GPa and 1100 °C for 3 hours to reach the basalt-olivine stability field. PC265 sample experienced the most massive Fe loss, due to the two successive loadings and piston-cylinder runs using two different Pt capsules. For clinopyroxene-feldspar/melt partitioning experiments, the starting sample was obtained from mixing 90 wt. % of previously synthesised glass with 10 wt. % feldspar (labradorite from Spectrum Mine, Plush, Lake Co., Oregon, courtesy of Marie Baïsset).

In situ partitioning measurements

In situ synchrotron experiments were conducted on beamline 16-BM-B at the Advanced Photon Source (Chicago, U.S.A.). High *P-T* conditions were generated using a Paris-Edinburgh press, with cell-assembly described in Yamada *et al.* (2011). An energy-dispersive X-ray set-up allowed the simultaneous collection of the diffraction and fluorescence signals on coexisting crystals and melt. To constrain the X-ray path length through the sample and preserve the sample cylindrical geometry, diamond capsules (inner diameter of 750 µm) were used and sealed under *P* by platinum-rhodium caps. MgO cylinder surrounding the graphite heater was modified with two boron-epoxy windows to reduce X-ray absorption for both the incident and diffracted X-rays. Temperature was calibrated from power-*T* curve calibrated against melting temperatures of salts (Kono *et al.*, 2014), and *P* was calculated from the cell volume of MgO (Kono *et al.*, 2010). Uncertainties on *P* and *T* are respectively 0.3 GPa and 80 °C. The design of the cell-assembly insures remarkable stability under high *P-T* conditions and a large vertical access to the sample throughout the experiment. At each *P-T* condition, an X-ray radiograph image of the sample was recorded (Fig. S-1), attesting that the whole sample could be probed through the anvil gap. Energy dispersive X-ray (EDX) data were collected on a Ge solid-state detector with slit size defining the X-ray beam of either 50 × 100 µm^2 or 100 × 100 µm^2, with collection time of 1800 s to 6700 s to optimise the signal to noise ratio for the Xe fluorescence peaks. EDX data were collected with the scattering angle (2-θ) at 10.0310 ± 0.0007°, or at 4.0285 ± 0.0005° if overlap of Xe fluorescence and Bragg diffraction peaks occurred at the higher 2-θ value. EDX data were processed by normalising intensities with live time, and slits size if different between datasets. Due to the lack of information on crystal preferential orientation using EDX, it is not possible to calculate crystal fraction from crystalline Bragg peaks area. Instead, EDX spectra collected on MgO at the same *P-T* conditions as crystal-melt equilibrium were taken as background intensity to calculate crystals *vs.* melt fraction from the intensity ratio between baselines from crystal-rich and melt patterns after background subtraction (Fig. S-2). In the case of Cell2, MgO and crystalline spectra have an overlapping baseline, indicating a melt content less than noise, *i.e.* less than 5 %.

Xenon concentrations were calculated from Xe K$_\alpha$ X-ray fluorescence line using the method described in Chen *et al.* (2022), where the absolute intensity of the fluorescence signal, I_i, depends on the following factors (Simabuco and Nascimento Filho, 1994): (1) beam intensity I_i^0, (2) Xe concentration in the sample $[\mathrm{Xe}]_i$, (3) average density ρ_i, (4) volume of the sample probed by the X-ray beam path V_i, (5) absorption by the sample and the surrounding cell-assembly A, and (6) detector sensitivity S as:

$$[\mathrm{Xe}]_i = \frac{I_i}{I_i^0 \times \rho_i \times V_i \times 10^{-A} \times S} \quad \text{(S-1)}$$

The factors I_i^0, A, and S are identical between crystal-rich and melt patterns. For both synchrotron runs, the sample was first fully molten at the targeted *P*, hence cell-assembly deformation between fully molten state and slightly cooled mineral-melt equilibrium state can be neglected, and Equation S-1 can be simplified to:

$$[\mathrm{Xe}]_i = [\mathrm{Xe}]_{\mathrm{fullmelt}} \times \frac{\Lambda_i}{\Lambda_{\mathrm{fullmelt}}} \times \frac{\rho_{\mathrm{fullmelt}}}{\rho_i} \quad \text{(S-2)}$$

with $[\mathrm{Xe}]_{\mathrm{fullmelt}}$ taken as the starting glass Xe content, and Λ the Xe K$_\alpha$ fluorescence peak area. Density of crystals and melts were calculated from (1) the Murnaghan equation of state and the thermal expansion for anorthite (Tribaudino *et al.*, 2010; Angel, 2004), (2) 3rd order Birch-Murnaghan equation of state for olivine (Liu and Li, 2006), (3) the high-*T* Birch-Murnaghan equation of state of diopside (Zhao *et al.*, 1998), and (4) from the 3rd order Birch-Murnaghan equation of state of mantle melts (Agee and Walker, 1988) and the compositional dependence from the ideal mixing model (Lange and Carmichael, 1987).

For datasets containing a mixture of melt and crystals, Xe weight fraction in crystals can be obtained from mass balance calculations:

$$[\mathrm{Xe}]_{\mathrm{c}} = \frac{[\mathrm{Xe}]_i - x_{i,\mathrm{m}}[\mathrm{Xe}]_{\mathrm{melt}}}{(1 - x_{i,\mathrm{m}})} \quad \text{(S-3)}$$

where $x_{i,\mathrm{m}}$ is the melt fraction in pattern *i*, and $[\mathrm{Xe}]_{\mathrm{melt}}$ is taken from the coexisting pure melt pattern.

Textural, chemical, and mineralogical analyses

Recovered sample images were obtained using a Zeiss Ultra 55 field emission scanning electron microscope (SEM), with a working distance of 7.5 mm and a voltage of 20 kV for detection of Xe. Note that samples recovered from present synchrotron experiments are all bubble free at the SEM scale (Fig. S-3). A few Xe submicron bubbles are observed inside olivine crystals from the additional basalt/olivine sample, although rarely. The major elements (Table S-1) of starting glass and recovered samples were determined using a Cameca SX-FIVE electron probe microanalyser (EPMA) on the Camparis platform at Sorbonne University. Accelerating voltage was set to 15 kV, with 5 nA beam current for Na, Ca, Al, Si and 40 nA for Xe. Note that in order to recover the samples from Paris-Edinburgh press experiments, diamond capsules had to be cracked and polished down. Xenon content in the starting glass was measured by EPMA using Xe calibration established following the procedure developed by Montana *et al.* (1993) by measuring the counts for the neighbouring elements, I (CuI) and Cs (CsCl).

Raman spectra were recorded on a JobinYvon Horiba HR460 spectrometer using a single-grating monochromator with 1500 gratings/mm and an argon laser (514.5 nm wavelength) to confirm the mineralogy of recovered samples (Fig. S-4) as obtained from EPMA analyses.

Mass spectrometry analyses

Xenon content on recovered glass pieces from Cell2, and both crystal-rich and glass pieces from run PC265, was measured by mass-spectrometry (Table S-2). Mass spectrometry (MS) measurements were done at the PIAGARA platform (LP2i-Bordeaux). The samples were beforehand weighted using a CAHN/Ventron 21 automatic electro-balance after performing the mandatory daily calibration. Although this electro-balance is precise down to 0.1 µg (for sample below 2 mg), a ±1 µg error is considered to take into account sample contamination or conversely surface erosion by handling.

The MS employed for the analyses is originally a model 1202 of V. G. Micromass 12 (magnetic sector, 60° deflection, and 12 cm radius instrument), incorporating in a small interior volume and customised with a Nier-type source (from a VG3000) and a Cu-Be electron multiplier detector for quantification (integration counting mode). Each sample was placed in an ultra-high vacuum chamber (below 10^{-8} mbar) and a laser was focused on the base of the sample holder (a Mo crucible, previously annealed at circa 2000 °C under vacuum to eliminate any possible Xe contamination). Description of the laser heating setup is reported in (Horlait *et al.*, 2021). A light laser power was first applied for few minutes to bring the sample and base holder at 50–100 °C in order to check for the presence of atmospheric contamination (physical sorption). For all three measured samples (seven fragments in total), no Xe was detected above the usual blank (few 10^5 of each major Xe isotope) after this pre-heating treatment. The sample fragment was then melted by progressively increasing the laser power. A camera is used to monitor sample evolution and the latter is considered melted once its original form changed to a round shape. After the visual observation of melting, the laser power was still conservatively increased by ~10 % and let steady for a few tens of seconds. For the tiniest samples (1 or 4 µg, see Table S-2), laser power obtained when melting larger sample fragments were applied. The evolved gas was treated by hot metallic powders to trap non-noble gases species and thus let only Xe into the MS setup (Horlait *et al.*, 2021). After a rapid estimation of Xe content by MS with a tiny fraction of the gas released from melted samples, the remaining fraction was spiked with a known amount of a monoisotopic ^{131}Xe gas before introduction in the MS. Xenon content from the sample was then deduced from the ^{i}Xe/^{131}Xe intensity ratios measured by MS. This approach allows reducing MS measurements errors to circa 5 % (main sources of errors stem from uncertainties of pipes volumes and spike ^{131}Xe content). As required the FileMaker sheet compiling raw MS measurements are given in MS Datasheets S-1 to S-7. Individual [Xe] values determined by MS and electro-balance measurements are listed in Table S-2.

Supplementary Tables

Table S-1 Chemical analyses of starting and quenched samples (wt. %). Note that Fe loss may have occurred at two stages, during Xe-doping using platinum capsules in piston-cylinder press experiments which is particularly strong for PC265 due to the successive use of two Pt capsules, and during synchrotron experiments due to Pt-Rh caps used to seal diamond capsules.

Sample	Na_2O	FeO	CaO	MgO	SiO_2	Al_2O_3	Totals
Xe-doped glass	–	12.54	13.47	10.44	45.14	17.24	99.22
		(0.25)	(0.26)	(0.18)	(0.59)	(0.16)	(1.15)
Cell2 quenched glass	–	4.88	15.27	13.07	49.08	18.79	101.31
		(0.19)	(0.28)	(0.22)	(0.52)	(0.26)	(0.73)
Cell2 olivine	–	8.81	0.35	51.12	42.26	0.10	102.75
		(0.87)	(0.06)	(1.16)	(0.45)	(0.05)	(1.1)
PC265 quenched glass	–	3.40	13.77	9.82	48.84	21.21	97.21
		(0.11)	(0.18)	(0.12)	(0.35)	(0.28)	(0.66)
PC265 olivine	–	0.42	0.45	55.83	44.09	0.44	101.41
		(0.61)	(0.29)	(0.96)	(0.66)	(0.35)	(0.71)
Cell3 quenched glass	0.95	0.28	14.52	12.16	49.26	19.62)	96.91
	(0.04)	(0.04)	(0.16)	(0.52)	(0.60)	(0.51)	(0.72)
Cell3 anorthite	1.87	0.17	17.30	0.93	48.77	30.47	99.65
	(0.11)	(0.03)	(0.63)	(0.06)	(0.28)	(1.97)	(0.78)
Cell3 diopside	0.18	0.42	14.96	26.91	53.32	9.29	105.34
	(0.04)	(0.36)	(0.97)	(1.13)	(0.090)	(1.15)	(0.41)

Table S-2 Mass spectrometry analyses. Errors on the Xe contents (from the variance of individual measurements) are given in brackets and refer to the last digit(s) of the corresponding value. Weighted averaging of Xe contents were done by pondering each value by the inverse square of its relative error. To better reflect that dispersion of results from a fragment to another presumably comes from samples heterogeneity rather than from Xe content measurements uncertainties, the errors in the last column are calculated from the variance against the average value of the individual Xe content values.

Analysis	Phase	Weight (μg)	Xe content (wt. %)
Cell2, piece 1	glass	57	1.84(7) × 10^{-3}
Cell2, piece 2	glass	65	1.42(6) × 10^{-3}
Cell2	**glass average**		**1.65(15)** × 10^{-3}
PC265, piece 1	glass	16	8.9(4) × 10^{-5}
PC265, piece 2	glass	1	9.4(4.7) × 10^{-5}
PC265, piece 3	glass	18.8	3.7(2) × 10^{-4}
PC265	**glass average**		**1.5(8)** × 10^{-4}
PC265, piece 4	olivine-rich	4	2.0(6) × 10^{-2}
PC265, piece 5	olivine-rich	4	4.8(1.5) × 10^{-3}
PC265	**olivine-rich average**		**1.3(5)** × 10^{-2}

Supplementary Figures

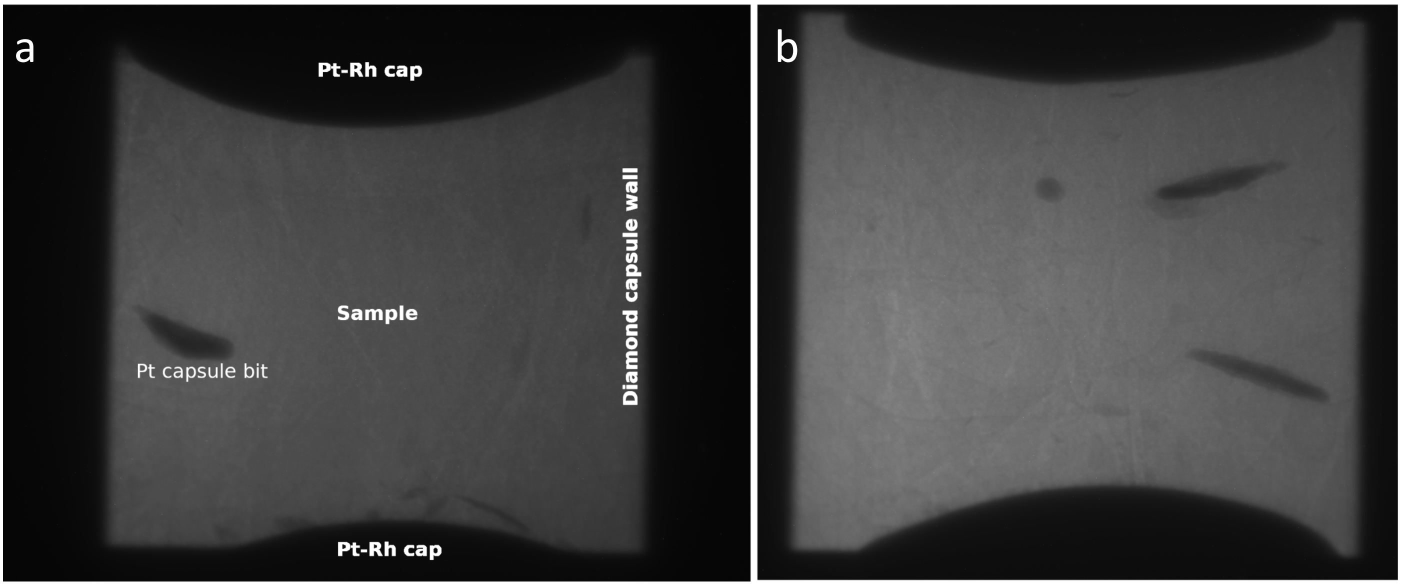

Figure S-1 X-ray radiographs taken at crystals-melt equilibrium and after quenching to room *T* at high *P*. **(a)** olivine/melt experiment (Cell2), **(b)** pyroxene-feldspar/melt experiment (Cell3). Sample width: 750 µm. Thin darker zones on radiographs are Pt bits that fell of the Pt capsule upon retrieving the starting Xe-doped glass.

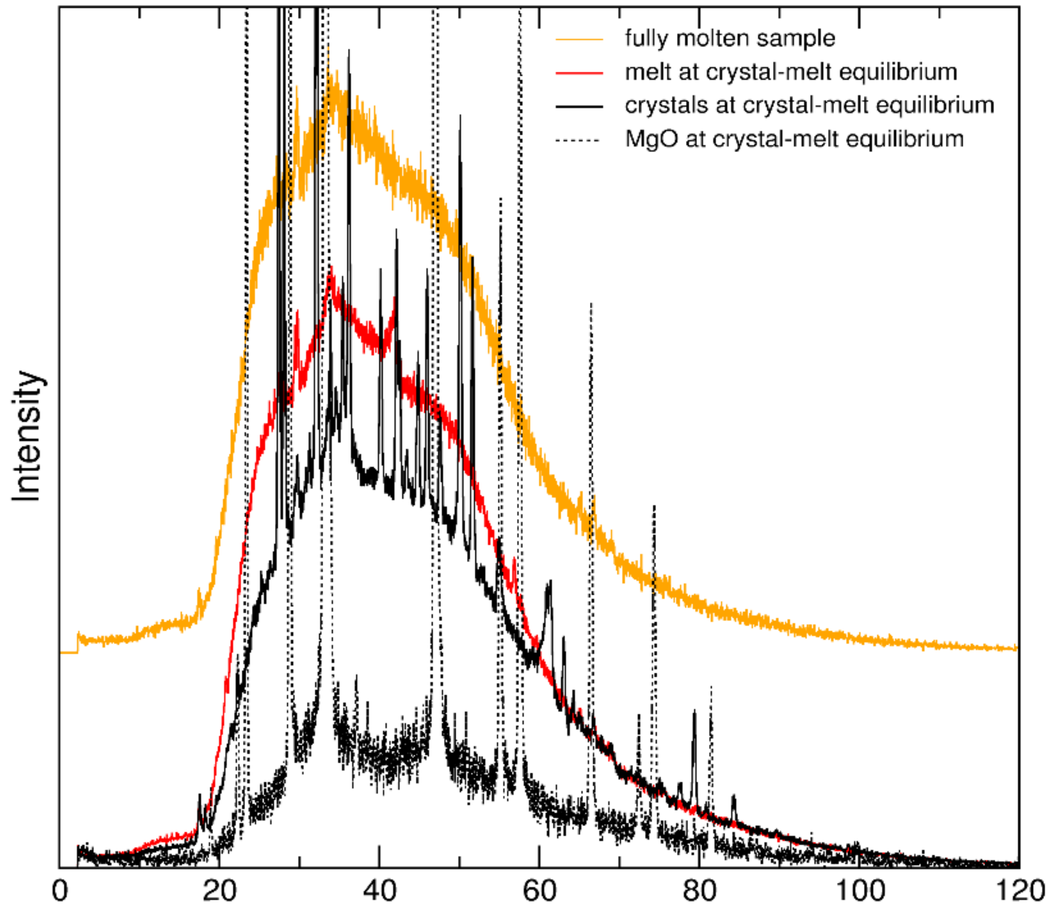

Figure S-2 EDX data collected at 10.031° on anorthite + diopside/melt equilibrium at 1.2 GPa and 1120 °C (Cell3), along with MgO dataset collected at the same *P-T* conditions, and taken as background intensity to calculate crystals *vs.* melt fraction (34(4) % crystals for this dataset) from the intensity ratio between baselines from crystal-rich and melt patterns after background subtraction.

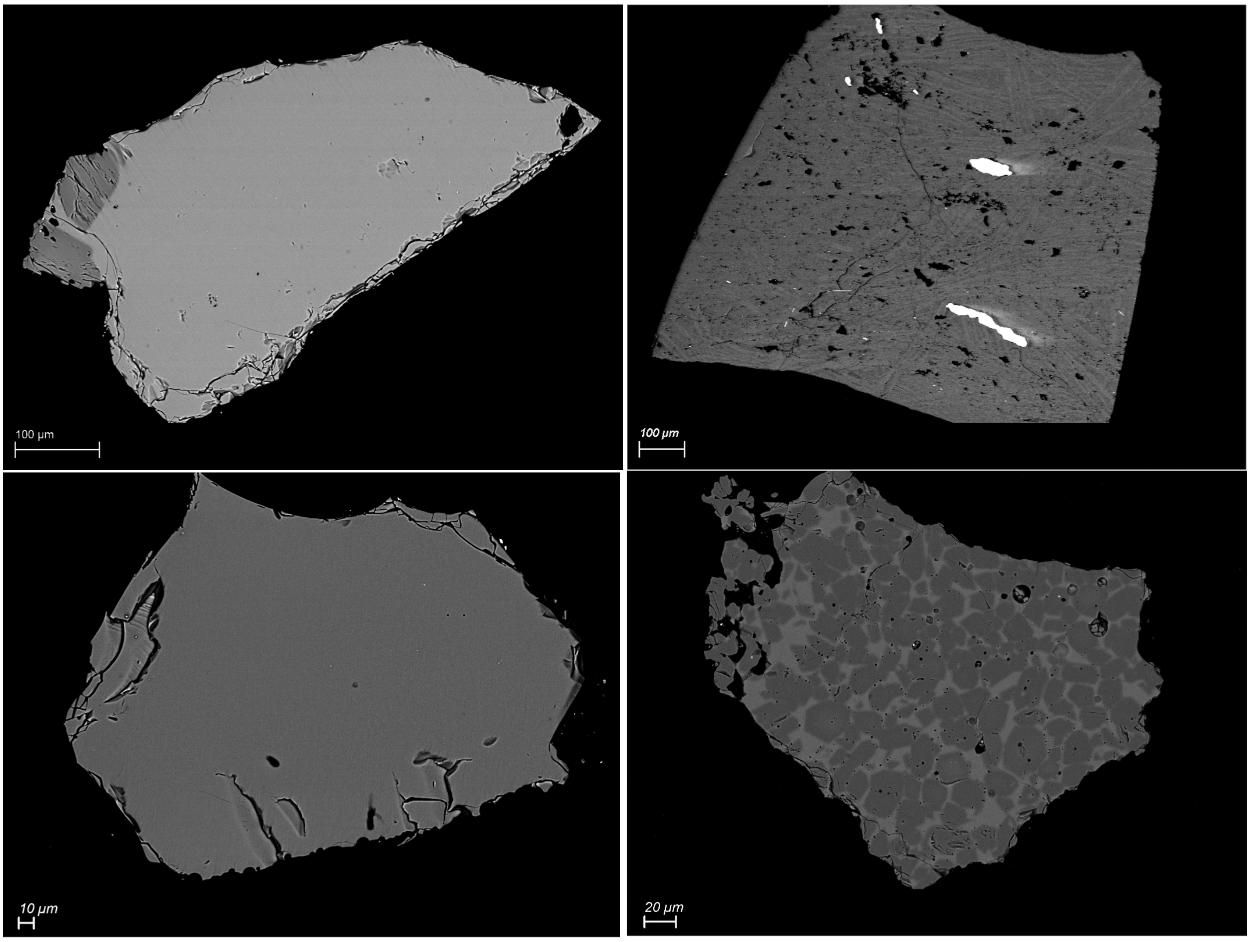

Figure S-3 SEM images of quenched samples. Top left: recovered sample piece from the olivine/melt experiment (Cell2) with two visible olivine crystals. Top right: whole recovered sample from the pyroxene-feldspar/melt experiment (Cell3), with mostly small size crystals and a fully glassy zone on the left hand side; bright zones are Pt bits that fell of the Pt capsule used to synthesise the starting Xe-doped glass. Bottom: sample slices from the olivine/melt additional experiment (PC265) used for mass-spectrometry analyses (pure glass on the left and mostly olivine crystals on the right).

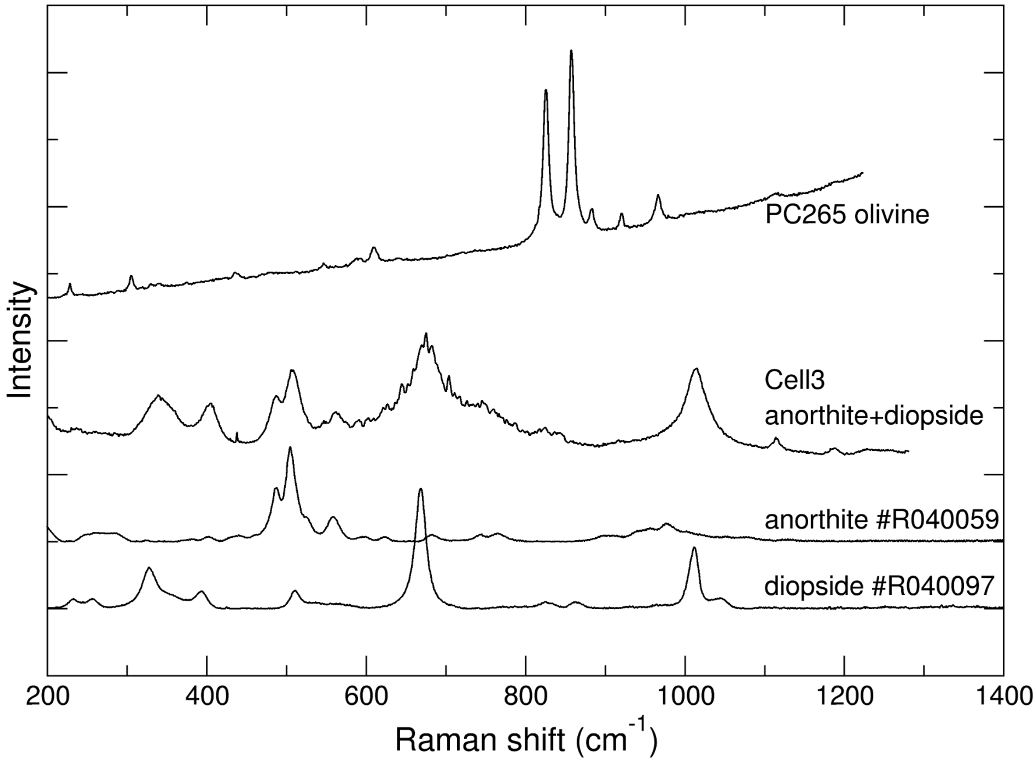

Figure S-4 Raman spectra collected on recovered samples from Cell3 and PC265. Spectra from RRUFF database (Lafuente *et al.*, 2016) are shown for comparison and identification of diopside and anorthite.

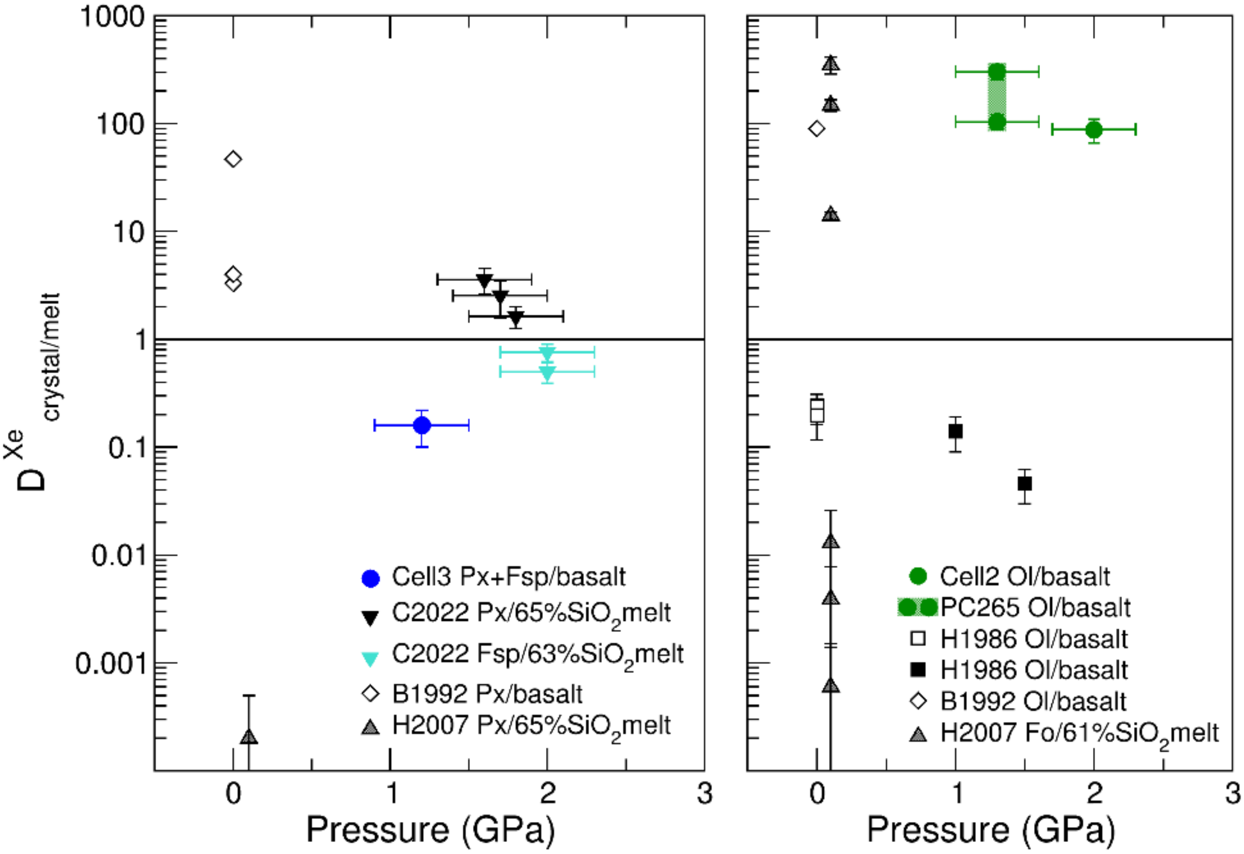

Figure S-5 Xenon crystal/melt partition coefficients as a function of pressure (left, pyroxene-feldspar/melt; right, olivine/melt). Data abbreviations: H1986, Hiyagon and Ozima (1986); B1992, Broadhurst *et al.* (1992); H2007, Heber *et al.* (2007); C2022, Chen *et al.* (2022); PC265, Cell2, and Cell3 are data from this study (Table 2). Note that Heber *et al.* (2007) discarded all values above unity due to the observation of gas bubbles in crystals.

Supplementary MS datasheets

Datasheet S-1 Annotated datasheet displaying the mixing of the Xe gas obtained from the melting of the sample "Cell2, piece 1" (see Table S-2) mixed with a precisely known ^{131}Xe monoisotopic reference gas. As explained in the previous section of this document, the measurement by MS of the $^{i}Xe/^{131}Xe$ ratios in the "sample + reference" gas mix allows to precisely deduce the Xe amount in the sample, without having to determine the sensitivity of the MS.

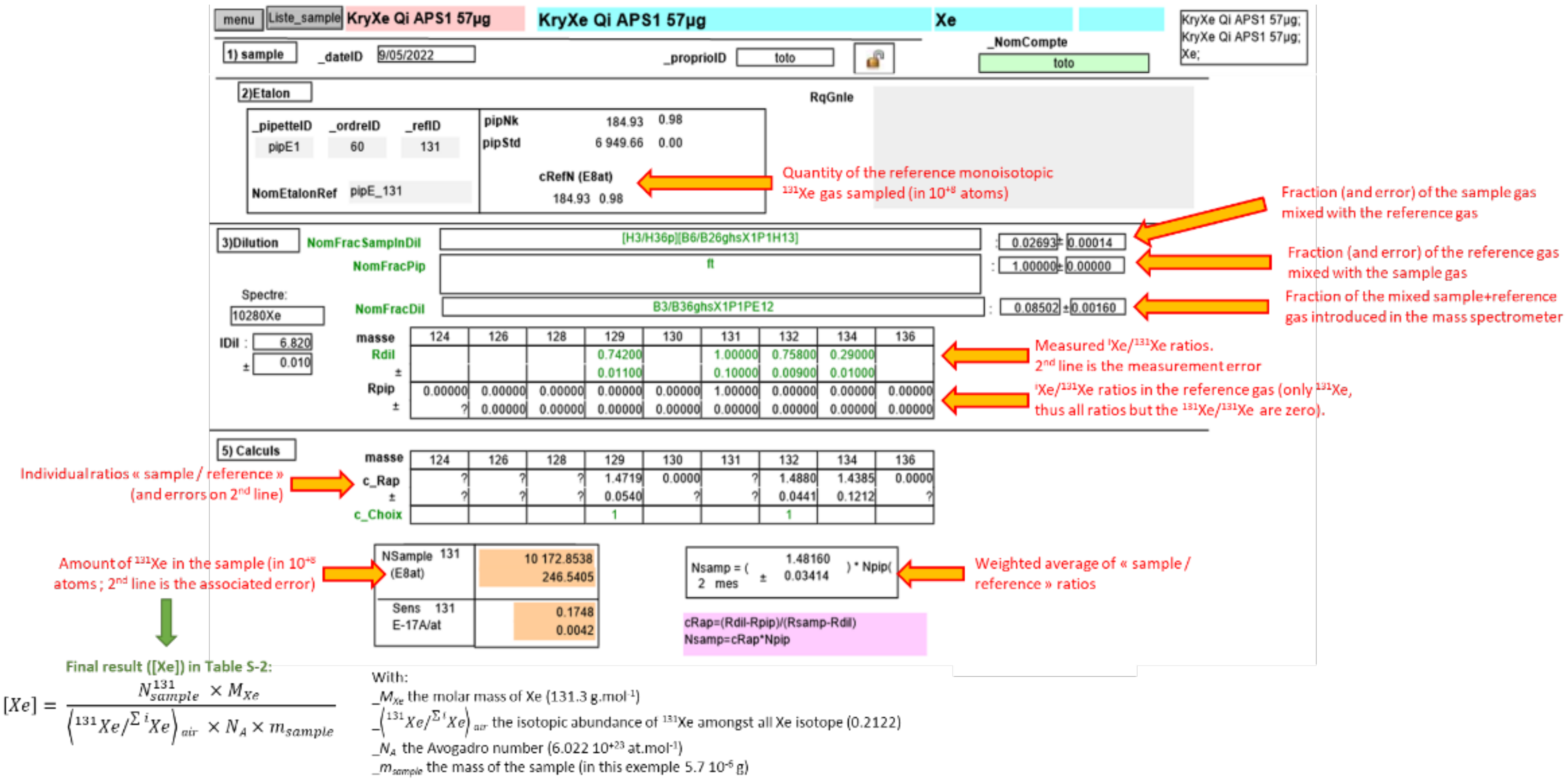

Datasheet S-2 MS datasheet for sample "Cell2, piece 2" (see Table S-2). For details, refer to annotated Datasheet S-1 and its caption.

menu | Liste_sample | KryXe Qi APS1 65µg | KryXe Qi APS1 65µg | Xe

KryXe Qi APS1 65µg; KryXe Qi APS1 65µg; Xe;

1) sample _dateID 12/05/2022 _proprioID toto _NomCompte toto

2)Etalon RqGnle

_pipetteID	_ordreID	_refID
pipE1	61	131

NomEtalonRef pipE_131

pipNk	184.86	0.98
pipStd	1 650.59	0.00

cRefN (E8at)
184.86 0.98

3)Dilution

NomFracSampInDil: B3/B26ghsH16pX1P1PE12 : 0.04440 ± 0.00086

NomFracPip: ft : 1.00000 ± 0.00000

Spectre: 10280Xe

NomFracDil: B3/B35ghsX1P1PE12 : 0.11251 ± 0.00207

lDil : 14.100 ± 0.010

masse	124	126	128	129	130	131	132	134	136
Rdil				0.86600		1.00000	0.86150	0.32850	
±				0.00700		0.10000	0.00500	0.00150	
Rpip	0.00000	0.00000	0.00000	0.00000	0.00000	1.00000	0.00000	0.00000	0.00000
±	?	0.00000	0.00000	0.00000	0.00000	0.00000	0.00000	0.00000	0.00000

5) Calculs

masse	124	126	128	129	130	131	132	134	136
c_Rap	?	?	?	2.2783	0.0000	?	2.1224	2.0141	0.0000
±	?	?	?	0.0607	?	?	0.0388	0.0303	?
c_Choix				1			1		

NSample 131 (E8at)	9 025.5905 346.3828
Sens 131 E-17A/at	0.2140 0.0063

Nsamp = (2.16773 ± 0.07078) * Npip(
2 mes

cRap=(Rdil-Rpip)/(Rsamp-Rdil)
Nsamp=cRap*Npip

Datasheet S-3 MS datasheet for sample "PC265, piece 4" (see Table S-2). For details, refer to annotated Datasheet S-1 and its caption.

menu | Liste_sample | KryXe Qi PC265 cryst1 | KryXe Qi PC265 cryst1 | Xe

KryXe Qi PC265 cryst1;KryXe Qi PC265 cryst1;Xe;

1) sample _dateID 14/04/2022 _proprioID toto _NomCompte toto

2)Etalon RqGnle

_pipetteID	_ordreID	_refID
pipE1	56	131

NomEtalonRef pipE_131

pipNk	185.24	0.98
pipStd	185.71	0.00

cRefN (E8at)
185.24 0.98

3)Dilution

NomFracSampInDil: Bg/B26ghsH16p : 0.01669 ± 0.00012

NomFracPip: ft : 1.00000 ± 0.00000

Spectre:

NomFracDil: B23/B25ghsX1P1PE12 : 0.15950 ± 0.00245

lDil : 11.000 ± 0.010

masse	124	126	128	129	130	131	132	134	136
Rdil				0.52000		1.00000	0.52500		
±				0.05000		0.00100	0.05000		
Rpip	0.00000	0.00000	0.00000	0.00000	0.00000	1.00000	0.00000	0.00000	0.00000
±	?	0.00000	0.00000	0.00000	0.00000	0.00000	0.00000	0.00000	0.00000

5) Calculs

masse	124	126	128	129	130	131	132	134	136
c_Rap	?	?	?	0.7162	0.0000	?	0.7072	0.0000	0.0000
±	?	?	?	0.1182	?	?	0.1150	?	?
c_Choix				1			1		

NSample 131 (E8at)	7 896.1940 917.3672
Sens 131 E-17A/at	0.2175 0.0111

Nsamp = (0.71154 ± 0.08241) * Npip(
2 mes

cRap=(Rdil-Rpip)/(Rsamp-Rdil)
Nsamp=cRap*Npip

Datasheet S-4 MS datasheet for sample "PC265, piece 5" (see Table S-2). For details, refer to annotated Datasheet S-1 and its caption.

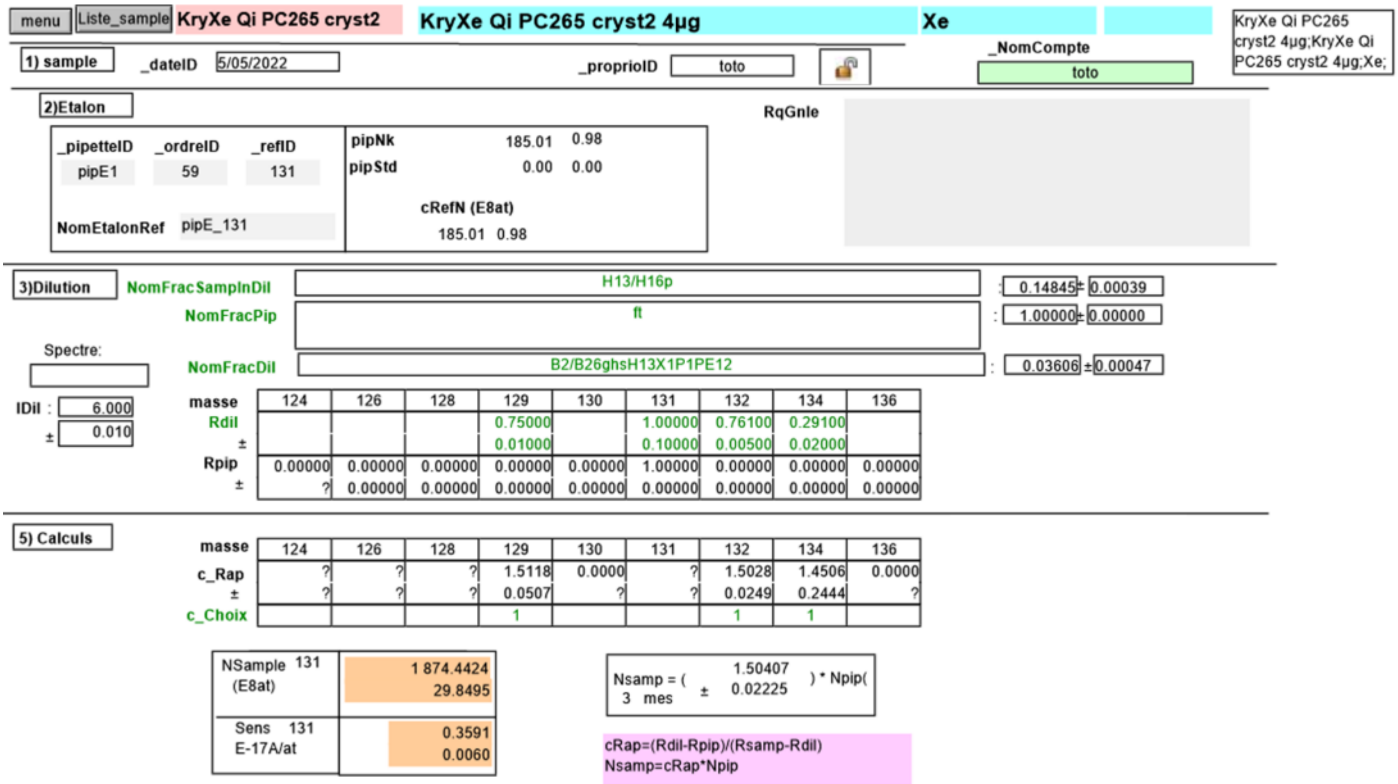

menu | Liste_sample | KryXe Qi PC265 cryst2 | KryXe Qi PC265 cryst2 4µg | Xe

KryXe Qi PC265 cryst2 4µg;KryXe Qi PC265 cryst2 4µg;Xe;

1) sample _dateID 5/05/2022 _proprioID toto _NomCompte toto

2)Etalon

_pipetteID	_ordreID	_refID
pipE1	59	131

NomEtalonRef pipE_131

pipNk 185.01 0.98
pipStd 0.00 0.00

cRefN (E8at) 185.01 0.98

RqGnle

3)Dilution

NomFracSampInDil H13/H16p : 0.14845 ± 0.00039
NomFracPip ft : 1.00000 ± 0.00000
Spectre:
NomFracDil B2/B26ghsH13X1P1PE12 : 0.03606 ± 0.00047

IDil : 6.000 ± 0.010

masse	124	126	128	129	130	131	132	134	136
Rdil				0.75000		1.00000	0.76100	0.29100	
±				0.01000		0.10000	0.00500	0.02000	
Rpip	0.00000	0.00000	0.00000	0.00000	0.00000	1.00000	0.00000	0.00000	0.00000
±	?	0.00000	0.00000	0.00000	0.00000	0.00000	0.00000	0.00000	0.00000

5) Calculs

masse	124	126	128	129	130	131	132	134	136
c_Rap	?	?	?	1.5118	0.0000	?	1.5028	1.4506	0.0000
±	?	?	?	0.0507	?	?	0.0249	0.2444	?
c_Choix				1			1	1	

NSample 131 (E8at) 1 874.4424 29.8495

Sens 131 E-17A/at 0.3591 0.0060

Nsamp = (1.50407 ± 0.02225) * Npip(3 mes

cRap=(Rdil-Rpip)/(Rsamp-Rdil)
Nsamp=cRap*Npip

Datasheet S-5 MS datasheet for sample "PC265, piece 1" (see Table S-2). For details, refer to annotated Datasheet S-1 and its caption.

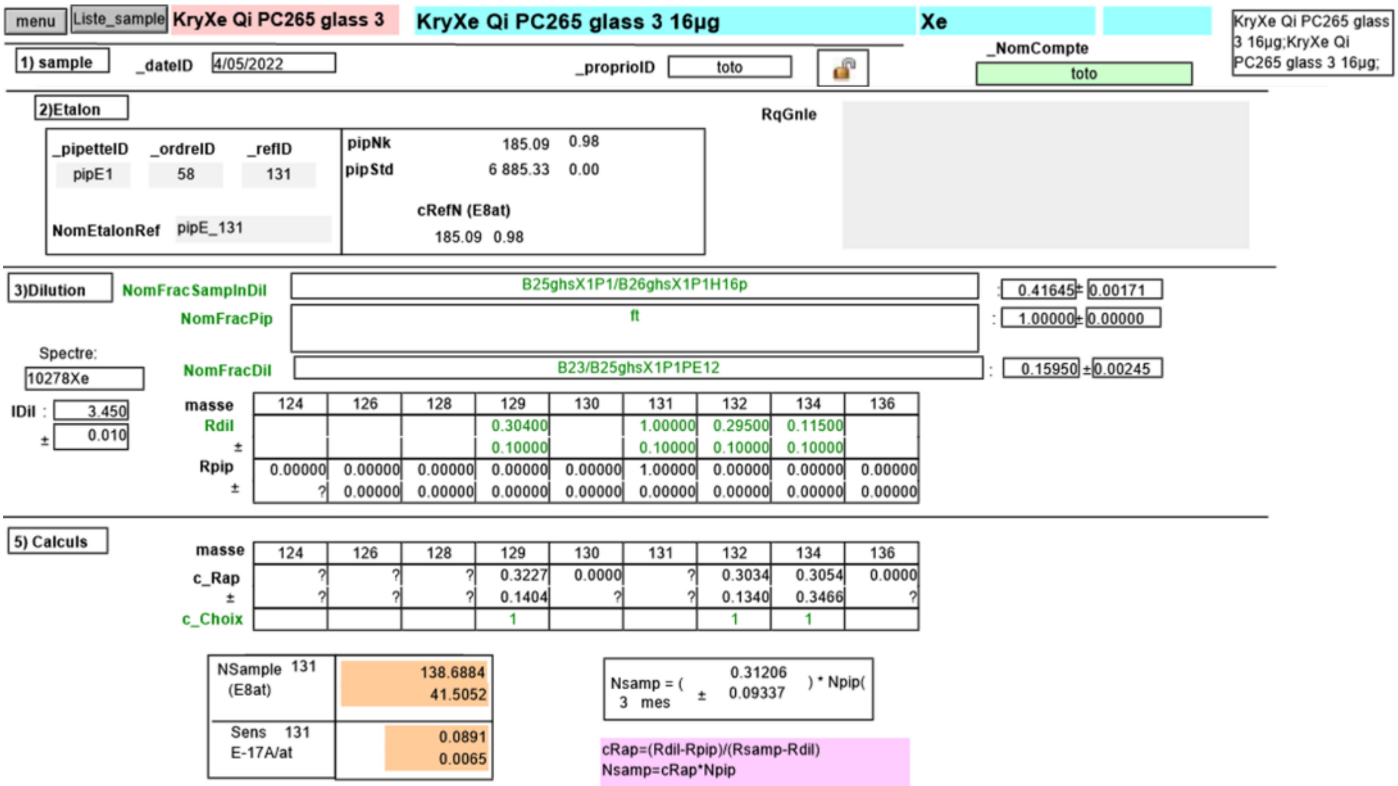

menu | Liste_sample | KryXe Qi PC265 glass 3 | KryXe Qi PC265 glass 3 16µg | Xe

KryXe Qi PC265 glass 3 16µg;KryXe Qi PC265 glass 3 16µg;

1) sample _dateID 4/05/2022 _proprioID toto _NomCompte toto

2)Etalon

_pipetteID	_ordreID	_refID
pipE1	58	131

NomEtalonRef pipE_131

pipNk 185.09 0.98
pipStd 6 885.33 0.00

cRefN (E8at) 185.09 0.98

RqGnle

3)Dilution

NomFracSampInDil B25ghsX1P1/B26ghsX1P1H16p : 0.41645 ± 0.00171
NomFracPip ft : 1.00000 ± 0.00000
Spectre: 10278Xe
NomFracDil B23/B25ghsX1P1PE12 : 0.15950 ± 0.00245

IDil : 3.450 ± 0.010

masse	124	126	128	129	130	131	132	134	136
Rdil				0.30400		1.00000	0.29500	0.11500	
±				0.10000		0.10000	0.10000	0.10000	
Rpip	0.00000	0.00000	0.00000	0.00000	0.00000	1.00000	0.00000	0.00000	0.00000
±	?	0.00000	0.00000	0.00000	0.00000	0.00000	0.00000	0.00000	0.00000

5) Calculs

masse	124	126	128	129	130	131	132	134	136
c_Rap	?	?	?	0.3227	0.0000	?	0.3034	0.3054	0.0000
±	?	?	?	0.1404	?	?	0.1340	0.3466	?
c_Choix				1			1	1	

NSample 131 (E8at) 138.6884 41.5052

Sens 131 E-17A/at 0.0891 0.0065

Nsamp = (0.31206 ± 0.09337) * Npip(3 mes

cRap=(Rdil-Rpip)/(Rsamp-Rdil)
Nsamp=cRap*Npip

Datasheet S-6 MS datasheet for sample "PC265, piece 2" (see Table S-2). For details, refer to annotated Datasheet S-1 and its caption.

menu | Liste_sample | KryXe Qi PC265 glass1 | **KryXe Qi PC265 glass1** | **Xe** | KryXe Qi PC265 glass1;KryXe Qi PC265 glass1;Xe;

1) sample _dateID 13/04/2022 _proprioID toto _NomCompte toto

2)Etalon RqGnle

_pipetteID	_ordreID	_refID
pipE1	54	131

NomEtalonRef pipE_131

pipNk	185.39	0.98
pipStd	248.25	0.00
cRefN (E8at)	185.39	0.98

3)Dilution

NomFracSampInDil ft : 1.00000 ± 0.00000

NomFracPip B23/B26ghsX1P1PE12H16 : 0.07454 ± 0.00123

Spectre:

NomFracDil B23/B26ghsH16p : 0.07060 ± 0.00117

IDil : 18.900 ± 0.010

masse	124	126	128	129	130	131	132	134	136
Rdil				0.51000		1.00000	0.49400		
±				0.10000		0.10000	0.10000		
Rpip	0.00000	0.00000	0.00000	0.00000	0.00000	1.00000	0.00000	0.00000	0.00000
±	?	0.00000	0.00000	0.00000	0.00000	0.00000	0.00000	0.00000	0.00000

5) Calculs

masse	124	126	128	129	130	131	132	134	136
c_Rap	?	?	?	0.6928	0.0000	?	0.6387	0.0000	0.0000
±	?	?	?	0.2300	?	?	0.2119	?	?
c_Choix				1			1		

NSample 131 (E8at)	9.1696 2.1592
Sens 131 E-17A/at	11.6461 1.1263

Nsamp = (0.66358 ± 0.15583) * Npip(2 mes

cRap=(Rdil-Rpip)/(Rsamp-Rdil)
Nsamp=cRap*Npip

Datasheet S-7 MS datasheet for sample "PC265, piece 3" (see Table S-2). For details, refer to annotated Datasheet S-1 and its caption.

menu | Liste_sample | Qi PC265 | **Qi PC265 18,8ug** | Qi PC265;Qi PC265 18,8ug;;

1) sample _dateID 23/05/2023 _proprioID toto _NomCompte toto

2)Etalon RqGnle

_pipetteID	_ordreID	_refID
pipE1	67	131

NomEtalonRef pipD1_m_82

pipNk	184.40	0.97	(E8at)
pipStd	0.00	0.00	(E8at)
cRefN (E8at)	184.40	0.97	(E8at)

3)Dilution

NomFracSampInDil B35fghrs/B15fghrsX12H2H67 : 0.29944 ± 0.00240

NomFracPip ft : 1.00000 ± 0.00000

Spectre:

NomFracDil B12/B15fghrsxy : 0.12627 ± 0.00137

IDil : 87.400 ± 0.200 nA

masse	124	126	128	129	130	131	132	134	136
Rdil			0.04942	0.66390	0.09759	1.00000	0.65980	0.25597	0.21720
±			0.00055	0.00230	0.00076		0.00300	0.00160	0.00130
Rpip	0.00000	0.00000	0.00000	0.00000	0.00000	1.00000	0.00000	0.00000	0.00000
±	0.00000	0.00000	0.00000	0.00000	0.00000	0.00000	0.00000	0.00000	0.00000

5) Calculs

masse	124	126	128	129	130	131	132	134	136
c_Rap	?	?	1.2060	1.1403	1.0359	?	1.0859	1.0863	1.0844
±	?	?	0.0296	0.0085	0.0164	?	0.0103	0.0142	0.0135
c_Choix				1		1	1	1	1

NSample 131 (E8at)	682.4361 10.5708
Sens 131 E-17A/at	1.7806 0.0246

Nsamp = (1.10820 ± 0.01348) * Npip(5 mes

cRap=(Rdil-Rpip)/(Rsamp-Rdil)
Nsamp=cRap*Npip

Supplementary Information References

Agee, C.B., Walker, D. (1988) Static compression and olivine flotation in ultrabasic silicate liquid. *Journal of Geophysical Research: Solid Earth* 93, 3437–3449. https://doi.org/10.1029/JB093iB04p03437

Angel, R.J. (2004) Equations of state of Plagioclase Feldspars. *Contributions to Mineralogy and Petrology* 146, 506–512. https://doi.org/10.1007/s00410-003-0515-5

Boettcher, S.L., Qiti, G., Montana, A. (1989) A simple device for loading gases in high-pressure experiments. *American Mineralogist* 74, 1383–1384. http://www.minsocam.org/ammin/AM74/AM74_1383.pdf

Broadhurst, C.L., Drake, M.J., Hagee, B.E., Bernatowicz, T.J. (1992) Solubility and partitioning of Ne, Ar, Kr, and Xe in minerals and synthetic basaltic melts. *Geochimica et Cosmochimica Acta* 56, 709–723. https://doi.org/10.1016/0016-7037(92)90092-W

Chen, Q., Sanloup, C., Bureau, H., Rzeplinski, I., Glazyrin, K., Farla, R. (2022) Probing the partitioning behaviour of Xe using *in situ* X-ray synchrotron techniques at high *P–T* conditions. *High Pressure Research* 42, 318–335. https://doi.org/10.1080/08957959.2022.2144290

Heber, V.S., Brooker, R.A., Kelley, S.P., Wood, B.J. (2007) Crystal-melt partitioning of noble gases (helium, neon, argon, krypton, and xenon) for olivine and clinopyroxene. *Geochimica et Cosmochimica Acta* 71, 1041–1061. https://doi.org/10.1016/j.gca.2006.11.010

Hiyagon, H., Ozima, M. (1986) Partition of noble gases between olivine and basalt melt. *Geochimica et Cosmochimica Acta* 50, 2045–2057. https://doi.org/10.1016/0016-7037(86)90258-9

Horlait, D., Faure, R., Thomas, B.A., Devert, N., Amany, M.-L., Carlot, G., Gilabert, E. (2021) A new thermo-desorption laser-heating setup for studying noble gases diffusion and release from materials at high temperatures. *Review of Scientific Instruments* 92, 124102. https://doi.org/10.1063/5.0068858

Kono, Y., Irifune, T., Higo, Y., Inoue, T., Barnhoorn, A. (2010) *P–V–T* relation of MgO derived by simultaneous elastic wave velocity and in situ X-ray measurements: A new pressure scale for the mantle transition region. *Physics of the Earth and Planetary Interiors* 183, 196–211. https://doi.org/10.1016/j.pepi.2010.03.010

Kono, Y., Park, C., Kenney-Benson, C., Shen, G., Wang, Y. (2014) Toward comprehensive studies of liquids at high pressures and high temperatures: Combined structure, elastic wave velocity, and viscosity measurements in the Paris-Edinburgh cell. *Physics of the Earth and Planetary Interiors* 228, 269–280. https://doi.org/10.1016/j.pepi.2013.09.006

Lafuente, B., Downs, R.T., Yang, H., Stone, N. (2016) 1. The power of databases: The RRUFF project. In: Armbruster, T., Danisi, R.M. (Eds.) *Highlights in Mineralogical Crystallography.* De Gruyter, Berlin, 1-30. https://doi.org/10.1515/9783110417104-003

Lange, R.A., Carmichael, I.S.E. (1987) Densities of Na_2O-K_2O-CaO-MgO-FeO-Fe_2O_3-Al_2O_3-TiO_2-SiO_2 liquids: New measurements and derived partial molar properties. *Geochimca et Cosmochimica Acta* 51, 2931–2946. https://doi.org/10.1016/0016-7037(87)90368-1

Liu, W., Li, B. (2006) Thermal equation of state of $(Mg_{0.9}Fe_{0.1})_2SiO_4$ olivine. *Physics of the Earth and Planetary Interiors* 157, 188–195. https://doi.org/10.1016/j.pepi.2006.04.003

Montana, A., Guo, Q., Boettcher, S., White, B.S., Brearley, M. (1993) Xe and Ar in high-pressure silicate liquids. *American Mineralogist* 78, 1135–1142. http://www.minsocam.org/ammin/AM78/AM78_1135.pdf

Sakai, R., Nagahara, H., Ozawa, K., Tachibana, S. (2014) Composition of the lunar magma ocean constrained by the conditions for the crust formation. *Icarus* 229, 45–56. https://doi.org/10.1016/j.icarus.2013.10.031

Simabuco, S.M., Nascimento Filho, V.F. (1994) Quantitative analysis by energy dispersive X-ray fluorescence by the transmission method applied to geological samples. *Scientia Agricola* 51, 197–206. https://doi.org/10.1590/S0103-90161994000200001

Tribaudino, M., Angel, R.J., Cámara, F., Nestola, F., Pasqual, D., Margiolaki, I. (2010) Thermal expansion of plagioclase feldspars. *Contributions to Mineralogy and Petrology* 160, 899–908. https://doi.org/10.1007/s00410-010-0513-3

Yamada, A., Wang, Y., Inoue, T., Yang, W., Park, C., Yu, T., Shen, G. (2011) High-pressure x-ray diffraction studies on the structure of liquid silicate using a Paris–Edinburgh type large volume press. *Review of Scientific Instruments* 82, 015103. https://doi.org/10.1063/1.3514087

Zhao, Y., Von Dreele, R.B., Zhang, J.Z., Weidner, D.J. (1998) Thermoelastic Equation of State of Monoclinic Pyroxene: $CaMgSi_2O_6$ Diopside. *The Review of High Pressure Science and Technology* 7, 25–27. https://doi.org/10.4131/JSHPREVIEW.7.25